Effects of Dip Angle on Rupture Propagation Along Branch Fault Systems

Evan Marschall*1 and Roby Douilly1 and Roby Doui

ABSTRACT

An important consideration in assessing seismic hazards is determining what is likely to happen when an earthquake rupture encounters a geometric complexity such as a branch fault. Previous studies showed parameters such as branch angle, stress orientation, and stress heterogeneity as key factors in the self-determined rupture path on branch faults. However, most of these studies were conducted in 2D or 3D with perfectly vertical faults. Therefore, in this study, we investigate the effects of dipping angle on rupture propagation along a branch fault system. We construct 3D finite-element meshes where we vary the dip angles (nine geometries in total) of the main and secondary faults, the stressing angle ($\Psi = 20^{\circ}$, 40°, and 65°), and the hypocenter location with nucleation on both the main and secondary segments. We find that for $\Psi = 40^{\circ}$, a rupture on the main fault is most likely to propagate across the branch intersection when the secondary fault is dipping. In addition, for $\Psi = 65^{\circ}$, a rupture on the secondary fault is most likely to propagate to the main fault when the secondary fault is shallowly dipping. This is caused by a fast rupture speed on the secondary fault and the dynamic stress effect that develops with the interaction of the free surface and the dipping secondary fault. These results indicate that dip angle is an important parameter in the determination of rupture path on branch fault systems, with potentially significant impact for seismic hazard, and should be considered in future dynamic rupture modeling studies.

KEY POINTS

- We use finite-element simulations to investigate dipangle effects on rupture along branching fault systems.
- Dip-slip faults induce free surface effects that may facilitate throughgoing rupture on branching faults.
- This may explain why some ruptures that start on smaller secondary faults may grow into larger earthquakes.

Supplemental Material

INTRODUCTION

It is well established that the size of an earthquake is proportional to the length of rupture (Aki, 1967; Kanamori, 1978). Geometric complexities along fault systems are features that can influence the total rupture length of an earthquake. Some examples include releasing and restraining bends (Woodcock and Fischer, 1986; Kadinsky-Cade and Barka, 1989; Lozos et al., 2011; Romanet et al., 2020), fault stepovers (Sibson et al., 1986; Harris et al., 1991; Harris and Day, 1999; Bai and Ampuero, 2017), and branch faults (Aochi et al., 2000, 2002; Kame et al., 2003; Bhat et al., 2007; Ma and Elbanna, 2019). All three can play important roles in rupture propagation, but in this study, we focus solely on branch faults.

There have been several large earthquakes that have occurred on branch fault systems with varying rupture behavior. Numerous examples exist where ruptures initiated on the main or secondary fault and propagated through the branch intersection, rupturing multiple fault segments. Such was the case for the 1979 $M_{\rm w}$ 6.5 Imperial Valley earthquake in southern California where the earthquake nucleated on the main Imperial fault and ruptured both the Imperial fault and the secondary Brawley fault segment (Archuleta, 1982, 1984). Another example is the recent 2023 $M_{\rm w}$ 7.8 Kahramanmaraş earthquake along the east Anatolian fault zone in Türkiye (Barbot et al., 2023; Melgar et al., 2023). In this case, rupture was initiated on the secondary Narlı fault and propagated through the branch intersection, rupturing ~300 km of the much larger main east Anatolian fault. Sometimes upon reaching a branch intersection, the rupture may continue only on one segment. As an example, the 2002 $M_{\rm w}$ 7.9 Denali earthquake nucleated on the Susitna Glacier thrust fault and

Cite this article as Marschall, E., and R. Douilly (2024). Effects of Dip Angle on Rupture Propagation Along Branch Fault Systems, *Bull. Seismol. Soc. Am.* **115**, 54–68, doi: 10.1785/0120240031

© Seismological Society of America

^{1.} University of California, Riverside, California, U.S.A., (a) https://orcid.org/0009-0003-0916-6656 (EM); (b) https://orcid.org/0000-0003-1724-2535 (RD)

^{*}Corresponding author: emars009@ucr.edu

ruptured the larger Denali transform fault. When the rupture reached the intersection between the Denali and Totschunda faults, the rupture transferred solely onto the Totschunda branch segment with no slip on the Denali fault past the branch intersection (Eberhart-Phillips *et al.*, 2003; Haeussler *et al.*, 2004; Ratchkovski *et al.*, 2004). Other times, the rupture is constrained to the nucleated fault at the discontinuity and does not rupture connecting faults. Such was the case for the 2010 $M_{\rm w}$ 7.0 Haiti earthquake, which nucleated on a blind thrust fault but did not rupture the main Enriquillo–Plantain Garden fault (Calais *et al.*, 2010; Douilly *et al.*, 2013). Understanding whether a rupture is likely to stop or propagate through a branch intersection is crucial for evaluating seismic hazards.

The complexity of rupture behavior on branch faults has led to many dynamic rupture studies highlighting several key parameters in the self-determination of rupture paths along branch fault systems. One such parameter is the angle between the main and secondary faults. Aochi et al. (2000) ran 3D dynamic rupture simulations for vertical branch faults and found smaller branch angles have larger stress shadowing effects which promote single-segment rupture; this effect diminishes with wider angles. Another important parameter in rupture selectivity on branch fault systems is whether the secondary branch is dilatational or compressional. Oglesby (2005) investigated rupture simulation on fault stepovers with an extensional and compressional linking dipping fault. He argued that the speed of the rupture as it encounters the branch segment and orientation of the dynamic stress fields which can cause clamping (increase in normal stress) or unclamping (decrease in normal stress) effects on a fault segment are important factors that can control whether a rupture will continue propagating beyond complex junctions. Because of this decrease in normal stress for the extensional fault and the increase in normal stress for the compressional case, they mentioned that it is easier for a rupture to propagate to an extensional (or dilatational) fault as opposed to a compressional fault. Although this is consistent with a wider stressing angle—the angle between the principal stress orientations and the main fault—(Aochi et al., 2002), a low stressing angle (less than 13°) can cause the rupture to favor the compressional branch instead of the dilatational branch. The orientation of the faults with respect to the regional stress field can also influence the rupture pattern on branch fault systems. Through 2D dynamic modeling, Kame et al. (2003) have shown that the rupture path that an earthquake takes at a branch is the result of the complex interplay between the fault geometry (i.e., branching angle), the background stress field before the earthquake (prestress), and the dynamic stress field radiated by the rupture front as it propagates along the fault system. Heterogenous on-fault stress is another parameter that influences the rupture path along branch faults. Duan and Oglesby (2007) show that over multiple earthquake cycles, a

heterogeneous fault stress field develops near a fault branch due to the interactions of the different segments. This heterogeneity in stresses can cause behaviors such as backward branching, in which the secondary fault has a delayed rupture after the rupture front passes the intersection, which can be different from the rupture anticipated in a simple stress field. All these studies lay a framework for understanding behavior along branch fault systems, but there are still some unanswered questions.

An important note about the earlier modeling studies is that they were either conducted in 2D or when conducted in 3D, they assumed a perfectly vertical fault and did not explore how a dipping fault might influence the outcome of the rupture. Douilly et al. (2020) investigated 3D rupture scenarios for the San Andreas fault in southern California focusing on the branched system of the eastern San Gorgonio Pass. Their study revealed that a slight change in fault geometry such as varying dip angle of faults could significantly impact the throughgoing rupture. This is particularly important because many natural complex fault systems have along-strike variations in dip. As an example, the dip angle of the San Andreas fault seems to vary significantly between several locations along the strike. Using potential field data, active source imaging, and seismicity, Fuis et al. (2012) suggest that the San Andreas fault appears to dip the southwest (55°-75°) northwest of the junction with the Garlock fault near the Big Bend area and transitions to steeply dipping northeast (80°) south of the intersection. The Alpine Fault in New Zealand is another example of a fault system with variable dip from steeply dipping to dipping as shallowly as 40° near Mt. Cook (Sibson et al., 1981; Kleffmann et al., 1998; Stern et al., 2007). Furthermore, recent seismic and geodetic inversions from the 2020 Elazığ earthquake have highlighted potential changes in a dip along the eastern Anatolian fault in Türkiye (Pousse-Beltran et al., 2020). Although many prominent strike-slip faults have variations in dip, the effects of dip on rupture near branch intersections have not been extensively explored.

Here, we conduct a 3D dynamic rupture modeling parameter study to investigate the effects of varying dip angles on the main and branch faults on rupture propagation. In this study, we experiment with various fault configurations, stress conditions, and hypocenter locations so that we can understand what effects dip angle may have on the rupture path along branch fault systems. Insights gained from this study will guide future rupture dynamics studies with complex fault geometries worldwide.

METHODS

The goal of our study is to highlight the effects that different dip angles have on rupture propagation along branch fault systems. We consider a branch fault system that has a 40-km-long planar main fault intersected by a 20 km secondary fault (Fig. 1). The branching angle (φ) between the main and

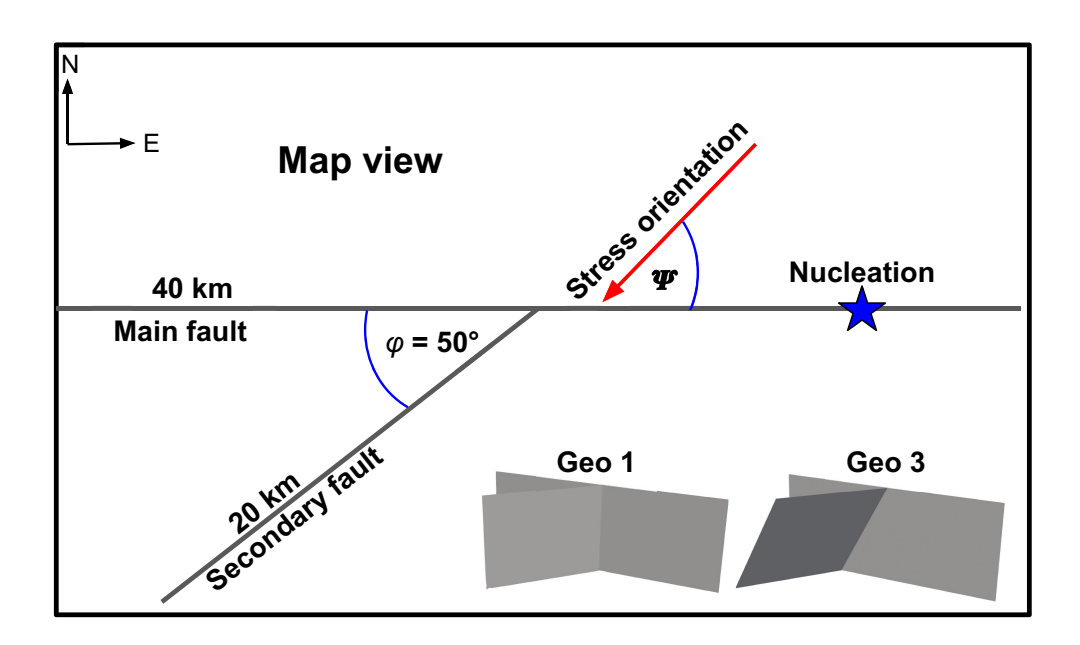


Figure 1. 2D schematic of the branch fault in map view. The main fault is 40 km long and is intersected by a 20 km secondary fault. The angle between the main and secondary fault (φ) is held constant at 50°. The red arrow indicates the angle of max horizontal stress (Ψ) relative to the main fault. The blue stars mark the nucleation location on the main and secondary faults (14 and 10 km from the intersection, respectively). In the lower section, there are 3D examples showing the difference between two of our geometries (Geo 1 and Geo 3). The color version of this figure is available only in the electronic edition.

secondary segment is held constant at 50°. The fault system is embedded in a homogenous, fully elastic half-space with a seismogenic depth of 15 km. In this study, we consider a range of values (90°, 75°, and 55°) for the dip angle on the main fault (D_M) and the secondary fault (D_B) , which leads to a total of nine unique geometries (Table 1). We construct 3D finiteelement meshes using the Cubit/Trelis meshing software and discretize the domain into tetrahedral elements with an onfault element size of 100 m which gradationally increases away from the fault. In our models, the nodes at the branch intersection belong to the main fault, which leads to a one-node spacing between the main and secondary fault at the intersection. We apply a smoothing condition to increase resolution and avoid singularities in the mesh (Knupp, 2000; Freitag and Knupp, 2002). For modeling the rupture propagation, we use the 3D finite-element code FaultMod (Barall, 2009), which has been validated in the Southern California Data Center community rupture code verification process (Harris et al., 2009, 2018). For the dynamic models, we consider three distinct stressing angles (angle of the maximum horizontal stress orientations relative to the main fault) ranging from inclination $(\Psi = 20^{\circ})$, low intermediate inclination $(\Psi = 40^{\circ})$, and high inclination ($\Psi = 65^{\circ}$) (Fig. 1). We choose those stressing angle to be able to compare our results with the 2D cases from Kame et al. (2003) and Bhat et al. (2007) and to understand whether the dip angle could have a significant impact on the rupture. To derive the initial shear and normal stresses on the faults, we first assume a strike-slip tectonic environment where the maximum principal stress (σ_1) and least principal stress (σ_3) are horizontal. We then rotate the system from the principal stress coordinate to the global coordinate system (east-north-

up), and we resolve stresses on each fault using the resulting stress tensor and apply a 12.5 MPa lithostatic overburden after rotation to prevent fault opening. Tables 2-4 detail the on-fault stresses and S values for each geometry for the three stressing angles ($\Psi = 20^{\circ}$, 40° , and 65°). The S value represents the ratio of fault strength to stress drop, a low S value promotes higher rupture speeds, and a high S value yields slower rupture speeds (Andrews, 1976; Das and Aki, 1977). In addition, the higher the S value, the farther away the fault is from failure and vice versa. The frictional behavior of the faults is governed by a linear slip-weakening friction law (Ida, 1972; Andrews, 1976) in which the frictional coefficient decreases from its static value (0.6) to its dynamic value (0.15) over a slip-weakening distance of 0.4 m. Rupture is nucleated by raising the shear stress in a circular patch of nodes, with a diameter of 4500 m to 10% above the failure strength of the fault to satisfy the critical patch size criteria for 3D dynamic models (Day, 1982). We also vary the nucleation location by considering nucleation on both the main and secondary faults.

TABLE 1 Branch Fault Geometries Tested in This Study									
Geometries	1	2	3	4	5	6	7	8	9
Main dip (D_M) Branch dip (D_B)	90°	90° 75°	90° 55°	75° 90°	75° 75°	75° 55°	55° 90°	55° 75°	55° 55°

TABLE 2 On-Fault Stresses for Every Geometry for Both the Main and Secondary Fault Under the $\Psi=$ 20° Stress Orientation

Geometry	Main σ _n (MPa)	Main τ (MPa)	Main S Value	Main Rake (°)	Secondary σ_n (MPa)	Secondary $ au$ (MPa)	Branch S Value	Secondary Rake (°)
Geo 1	14.84	6.43	0.59	180	17.5	8.66	0.30	0
Geo 2	14.84	6.43	0.59	180	17.93	8.9	0.30	-16
Geo 3	14.84	6.43	0.59	180	20.03	9.69	0.35	-35
Geo 4	16.03	7.62	0.38	215	17.5	8.66	0.30	0
Geo 5	16.03	7.62	0.38	215	17.93	8.9	0.30	-16
Geo 6	16.03	7.62	0.38	215	20.03	9.69	0.35	-35
Geo 7	20.65	9.83	0.38	238	17.5	8.66	0.30	0
Geo 8	20.65	9.83	0.38	238	17.93	8.9	0.30	-15
Geo 9	20.65	9.83	0.38	238	20.03	9.69	0.35	-35

The rake shown here is calculated from the initial up-dip and along-strike shear stresses on each fault segment.

TABLE 3 On-Fault Stresses for Every Geometry for Both the Main and Secondary Fault Under the $\Psi=40^\circ$ Stress Orientation

Geometry	Main σ_n (MPa)	Main τ (MPa)	Main S Value	Main Rake (°)	Secondary σ_n (MPa)	Secondary $ au$ (MPa)	Branch S Value	Secondary Rake (°)
Geo 1	20.76	9.85	0.39	180	13.1	3.42	3.05	0
Geo 2	20.76	9.85	0.39	180	13.67	4.68	1.34	-44
Geo 3	20.76	9.85	0.39	180	16.37	7.9	0.35	-67
Geo 4	21.55	9.96	0.44	197	13.1	3.42	3.05	0
Geo 5	21.55	9.96	0.44	197	13.67	4.68	1.34	-44
Geo 6	21.55	9.96	0.44	197	16.37	7.9	0.35	-67
Geo 7	24.62	9.77	0.82	214	13.1	3.42	3.05	0
Geo 8	24.62	9.77	0.82	214	13.67	4.68	1.34	-44
Geo 9	24.62	9.77	0.82	214	16.37	7.9	0.35	-67

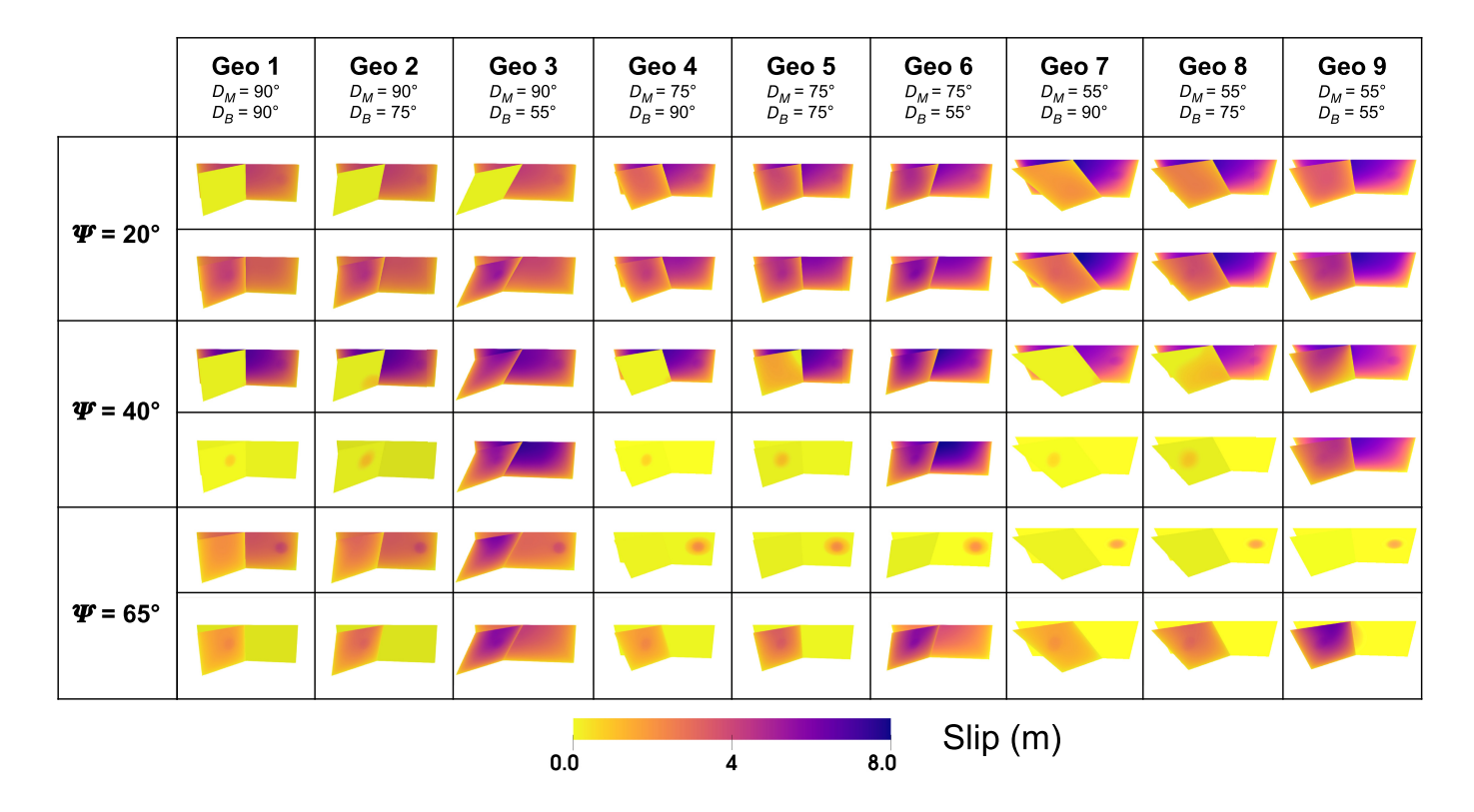
TABLE 4 On-Fault Stresses for Every Geometry for Both the Main and Secondary Fault Under the Ψ = 65° Stress Orientation

Geometry	Main σ_n (MPa)	Main $ au$ (MPa)	Main S Value	Main Rake (°)	Secondary σ_n (MPa)	Secondary $ au$ (MPa)	Branch S Value	Secondary Rake (°)
Geo 1	28.93	7.66	2.92	180	13.84	5.0	1.13	180
Geo 2	28.93	7.66	2.92	180	14.38	5.84	0.76	212
Geo 3	28.93	7.66	2.92	180	16.98	8.34	0.32	237
Geo 4	29.17	7.45	3.27	187	13.84	5.0	1.13	180
Geo 5	29.17	7.45	3.27	187	14.38	5.84	0.76	212
Geo 6	29.17	7.45	3.27	187	16.98	8.34	0.32	237
Geo 7	30.1	6.5	5.82	195	13.84	5.0	1.13	180
Geo 8	30.1	6.5	5.82	195	14.38	5.84	0.76	212
Geo 9	30.1	6.5	5.82	195	16.98	8.34	0.32	237

RESULTS

In this study, we run 54 simulations to investigate the rupture path on branch faults where we vary the dipping angles (nine geometries), the stressing angle (three inclinations), and the hypocenter location with nucleation on both the main and secondary segments. We observe several main outcomes

(Fig. 2): (1) rupture dies out shortly after nucleation, (2) the rupture only ruptures the nucleated fault, (3) the rupture causes some measurable slip on the non-nucleating fault, and (4) both faults fully rupture. Supplemental videos S1–S9, available in the supplemental material of this article, show the time-dependent slip evolution for each model presented



in Figure 2. In the subsequent sections, we will highlight the results from our simulations and compare them with the corresponding 2D cases from Kame *et al.* (2003).

Nucleation on Main Fault

The low inclination of the stressing angle ($\Psi = 20^{\circ}$).

On a vertical, planar branch fault system, the rupture path is mainly controlled by the rupture velocity, the stress state, and the fault branching angle (Poliakov et al., 2002; Kame et al., 2003; Bhat et al., 2004, 2007). Kame et al. (2003) and Bhat et al. (2007) argued that for low stressing angle, a 2D rupture will mostly favor the main fault and bypass the extensional branching fault regardless of the rupture speed. However, if the secondary fault is on the compressional side, when the rupture reaches the intersection, it will only continue onto the compressional secondary branch for low branching angle (φ < 15°) and low rupture speed. For a higher rupture speed (90% of shear-wave velocity or higher), the rupture could continue to the main fault, but it will die out after a short distance. But for a wide branching angle $(\varphi > 15^{\circ})$, a rupture will continue on both the main and compressional secondary segments regardless of the rupture speed. In our 3D case for a low stressing angle, when rupture is nucleated on a vertical main fault (geometries 1, 2, and 3; Fig. 2), the rupture only propagates on the main fault, passing the branching intersection without causing slip on the extensional secondary segment regardless of the dip on the secondary segment. This is consistent with the 2D results presented in Kame et al. (2003) and Bhat et al. (2007) and should also suggest that the rupture would have propagated on both fault segments if the secondary fault was on the compressional side. However, in

Figure 2. A collection of all slip results for the different geometries under the various stressing angles. For each stress angle, the top row shows results for nucleation on the main fault and the lower row shows results for nucleation on the secondary segment. The color version of this figure is available only in the electronic edition.

contrast to the vertical main fault, when the main fault is more shallowly dipping, the rupture propagates on both the main and secondary segments. Figure 3 shows the snapshots of the slip rate and final slip for geometries 1, 4, 7, and 9. Adding a nonvertical dip to the main fault causes a decrease in the *S* value of that fault that promotes a faster rupture speed on the main fault (see geometries 1 and 4 in Fig. 3). When the rupture reaches the junction when the main fault is shallowly dipping, the rupture propagates on the extensional secondary fault. However, there is a delay in triggering when the main fault is dipping at 75° compared to the 55° case, which is mostly likely due to the slower rupture speed of the 75° case.

Intermediate stressing angle ($\Psi=40^{\circ}$). Kame *et al.* (2003) also detailed the 2D rupture path scenarios for the intermediate stressing angle. They mentioned that the rupture will mostly favor the extensional branching fault regardless of the rupture speed for a low branching angle. When the rupture reaches the junction, it will fully rupture the extensional secondary branch but die out on the main fault for a lower rupture speed. For higher rupture speed, the rupture could fully break both segments. However, for a wider branching angle, a 2D rupture will favor the main fault and simultaneous rupture on both segments could occur for a larger rupture speed. In our 3D case,

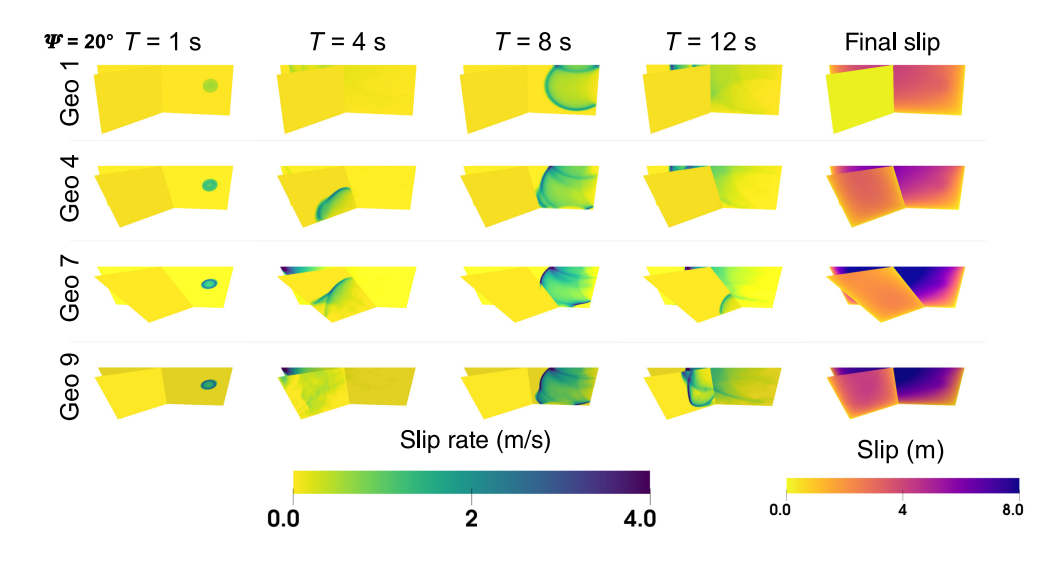


Figure 3. Snapshots showing slip rate for geometries 1, 4, 7, and 9 under the $\Psi=20^\circ$ stressing angle, as well as the final slip (last column) on the fault systems. When the main and secondary faults are both vertical (Geo 1), the rupture remains solely on the main fault. However, the rupture propagates onto the vertical secondary fault when the main fault is dipping (Geo 4 and Geo 7). A shallower dipping secondary fault promotes a higher slip magnitude (Geo 9). The color version of this figure is available only in the electronic edition.

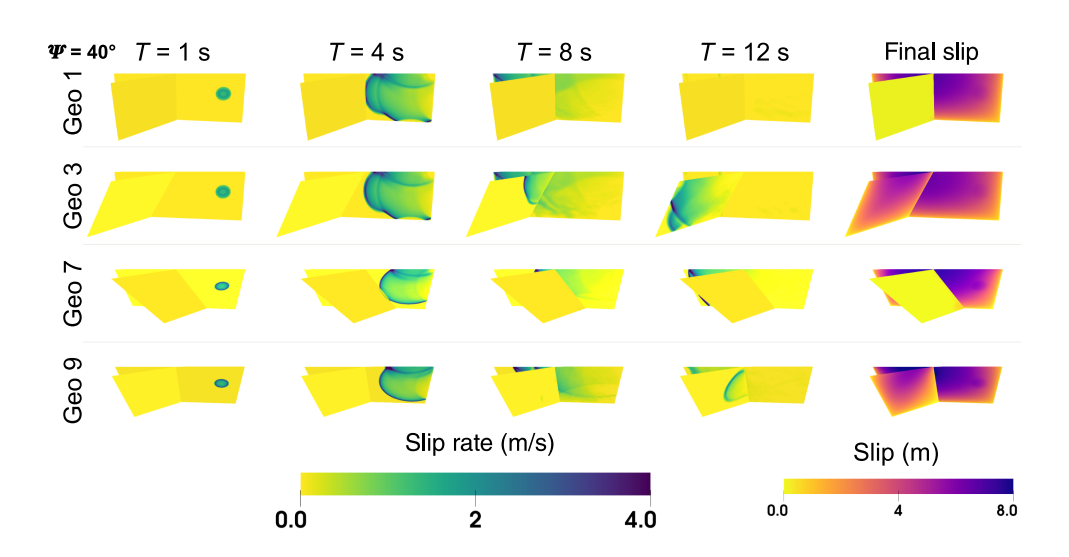


Figure 4. Snapshots showing slip rate for geometries 1, 3, 7, and 9 under the $\Psi=40^\circ$ stressing angle as well as the final slip (last column). When rupture is nucleated on the main fault, it only ruptures the secondary segment when the secondary fault is dipping 55° (Geo 3 and Geo 9). When the secondary fault is vertical (Geo 1 and Geo 7), it does not slip. The color version of this figure is available only in the electronic edition.

when both segments are vertical, the rupture favors the main fault consistently with the results of Kame *et al.* (2003). However, for the shallower dipping angle of the secondary fault (55°), the rupture fully propagates across both faults. For the 75° dipping secondary fault (see geometry 2 in Fig. 2), there is a small slip on the secondary fault, but the rupture quickly dies out. Figure 4 shows the time evolution of the slip rate and the final slip for geometries 1, 3, 7, and 9. For rupture on geometries 1 and 3, we could note that when the shallower dipping secondary fault

slips, it further increases the slip on the main fault near the branch intersection. Overall, decreasing the dip of the secondary fault causes the S value on that fault to decrease (the fault is closer to failure) and thus the increase in shear stress on that fault is enough to facilitate throughgoing rupture. For geometry 6 (vertical secondary fault), a shallowly dipping main fault leads to an increase in the S value on the main fault and thus a reduction of the rupture speed. Nevertheless, similar to geometry 1, the rupture still favors the main segment and completely bypasses the extenfault. sional secondary However, a slight change in the dip of the secondary fault (geometries 8 and 9 in Figs. 2 and 4) was enough to promote simultaneous rupture.

High stressing angle $(\Psi = 65^\circ)$. Kame et al. (2003) inferred that for a high stressing angle, a 2D rupture will mostly favor the extensional branching fault and not the compressional branch regardless of the rupture speed, where the rupture will only continue on the extensional secondary branch for a low branching angle, but the rupture could propagate on both segments for high rupture speed. On the other hand, for a wider branching angle, a rupture will continue on both the main and extensional secondary segments

regardless of the rupture speed. In our 3D case, when we initiate the rupture on a vertical main fault (geometries 1, 2, and 3), the rupture continues on both the main and secondary segments regardless of the dip on the secondary segment (Fig. 2) even for the large S value (S = 2.92) on the main fault. This result is consistent with the wide branch angle 2D cases of Kame *et al.* (2003). Figure 5 shows the rupture simulation on geometries 1, 2, and 3 for the stressing angle of 65°. We can observe that when the rupture reaches the branch intersection, the

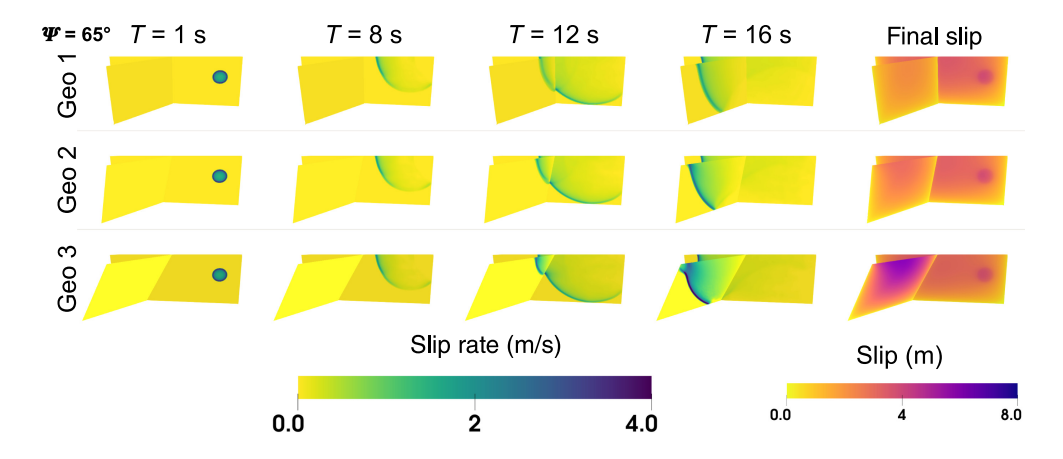


Figure 5. Snapshots showing slip rate for geometries 1, 2, and 3 under the $\Psi=65^{\circ}$ stressing angle, as well as the final slip on the fault systems for nucleation on the main fault. The rupture propagates onto the secondary fault for all geometries, but we see progressively more slip as the dip shallows from vertical (Geo 1), to 75° (Geo 2), and to 55° (Geo 3). The color version of this figure is available only in the electronic edition.

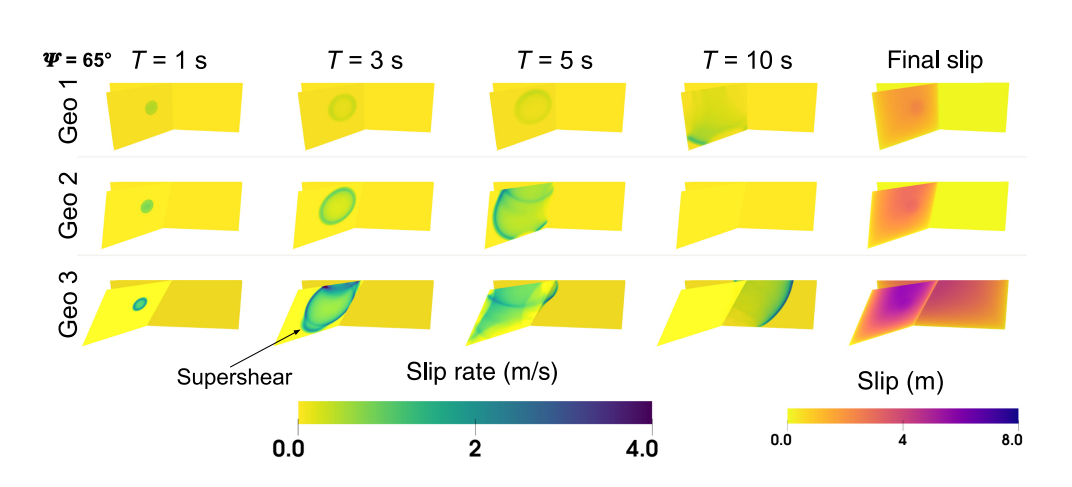


Figure 6. Snapshots showing slip rate for geometries 1, 2, and 3 under the $\Psi=65^{\circ}$ stressing angle as well as the final slip on the fault systems for nucleation on the secondary fault segment. The rupture only propagates onto the main fault for the 55° dipping angle case on the secondary segment where the rupture experiences supershear speeds (Geo 3). The color version of this figure is available only in the electronic edition.

secondary fault experiences more slip for shallower dipping secondary fault and thus the higher slip magnitude occurs when the secondary fault dips 55°. In addition, because slip on the secondary fault increases, more slip occurs on the main fault near the branching intersection on the hanging-wall side. When we make the dip of the main fault shallower, it increases the *S* value on the main fault, which then causes the rupture to die out quickly on the main fault after nucleation. For the main fault dipping 55° to the north, the slipping area is slightly larger than the 75° case, but for both cases, the slip patch is localized near the nucleation zone.

Nucleation on secondary fault

We notice that the dip angle has a stronger impact on throughgoing rupture when we initiate the rupture on the secondary fault as opposed to the main fault. This effect is more visible for the intermediate and highstressing angle cases. When rupture is nucleated on the secondary fault segment under the low stressing angle ($\Psi = 20^{\circ}$), the rupture propagates onto the main fault regardless of the dip angle (Fig. 2, second row). This is most likely because all these scenarios have low S values (fast rupture speed) that lead to supershear rupture. For the intermediate stressing angle $(\Psi = 40^{\circ})$, the rupture propagates fully to the main fault only when the secondary fault is shallowly dipping. For the vertical and 75° dipping secondary faults, the rupture dies out quickly nucleation. after However, when the branch fault is dipping at 55°, it has a much lower S value (Table 3), and the rupture propagates bilaterally on the main fault, regardless of the dip angle of the main fault.

Under the high stressing angle ($\Psi=65^{\circ}$) case, when rupture nucleates on the secondary fault, we observe several outcomes. For nucleation on vertical and 75° dipping secondary faults, the rupture is constrained to the secondary fault and does not propagate onto the main fault, regardless of the dip of the main fault. However, when the rupture

nucleates on the shallowly dipping secondary fault $(D_B=55^\circ)$, it propagates onto the main fault (Fig. 6). For geometries 3 $(D_M=90^\circ)$ and 6 $(D_M=75^\circ)$, the rupture initially propagates unilaterally on the main fault near the branch intersection, but ultimately ruptures bilaterally for both. For geometry 9 $(D_M=55^\circ)$, the rupture propagates across the branch intersection but did not fully break the main fault (Fig. 7). The throughgoing rupture scenarios are partly due to a fast rupture speed when the secondary fault is dipping at 55° that cause the rupture to be supershear on that segment (see Fig. 6). It is important to notice that for this high stressing angle case, the S value on the main value increases (fault is moving away from failure) because the dip of that fault increases. When the main fault dips at 75° or 55°, any rupture initiated on the main fault dies out very quickly due to the high S values (Table 4).

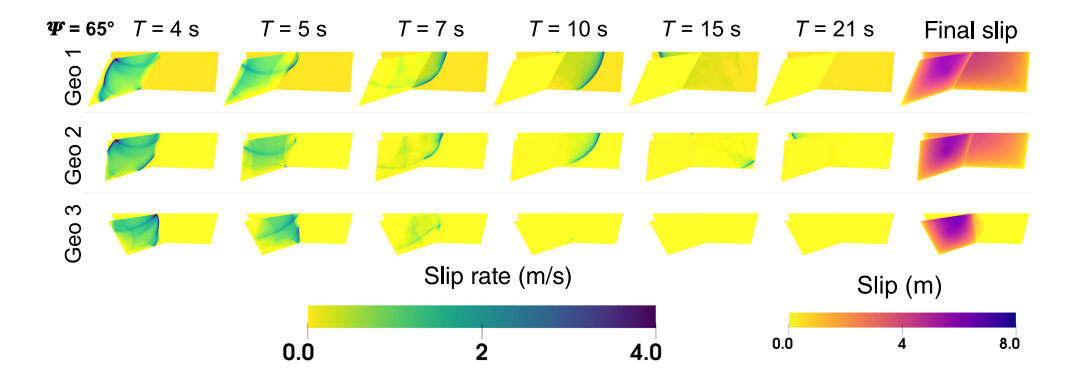


Figure 7. Snapshots showing slip rate for geometries 3, 6, and 9 under the $\Psi=65^{\circ}$ stressing angle. When rupture is nucleated on the shallow dipping secondary fault, it causes a slip on the main fault. When the main fault is dipping 55°, the rupture quickly dies out after the branch intersection. For steeper and vertical main faults (Geo 3 and Geo 6), the rupture continues bilaterally on the main fault. The color version of this figure is available only in the electronic edition.

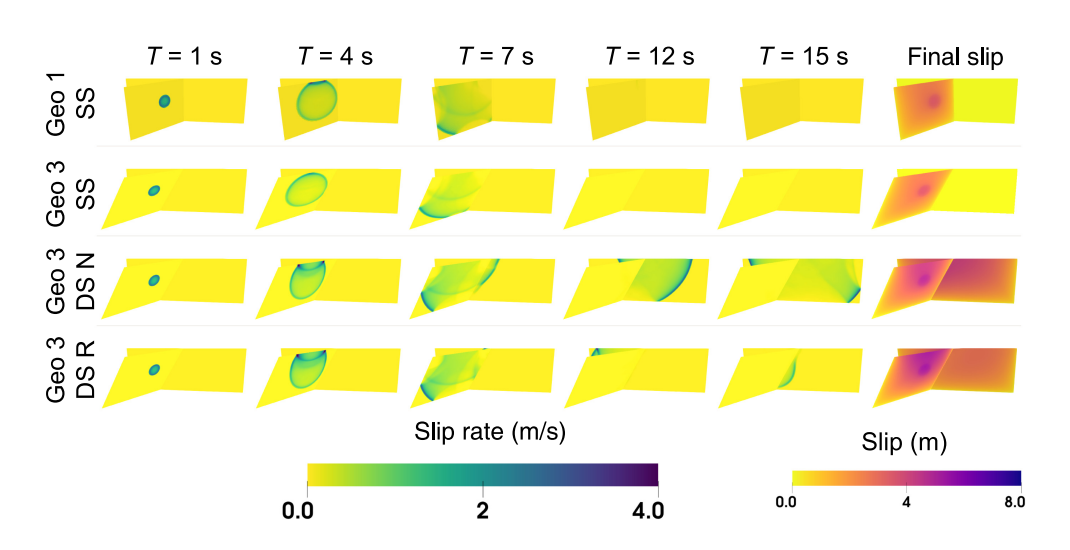


Figure 8. Snapshots showing slip rate for geometry 1 SS (purely left-lateral strike-slip), geometry 3 SS (purely left-lateral strike-slip), geometry 3 DS N (purely normal dip-slip), and geometry 3 DS R (purely reverse dip-slip) with 25 MPa normal stress and 7.5 MPa shear stress. For all geometries, the rupture reaches the branch intersection, but it only propagates onto the main fault when the secondary fault has a dip-slip motion (Geo 3 DS N and Geo 3 DS R). The color version of this figure is available only in the electronic edition.

Therefore, the fact that rupture is only able to propagate through the branch intersection when it nucleates on the shallowest dipping secondary fault suggests that the dip angle and the faster rupture speed promote slip on the main fault despite its high *S* value.

DISCUSSION

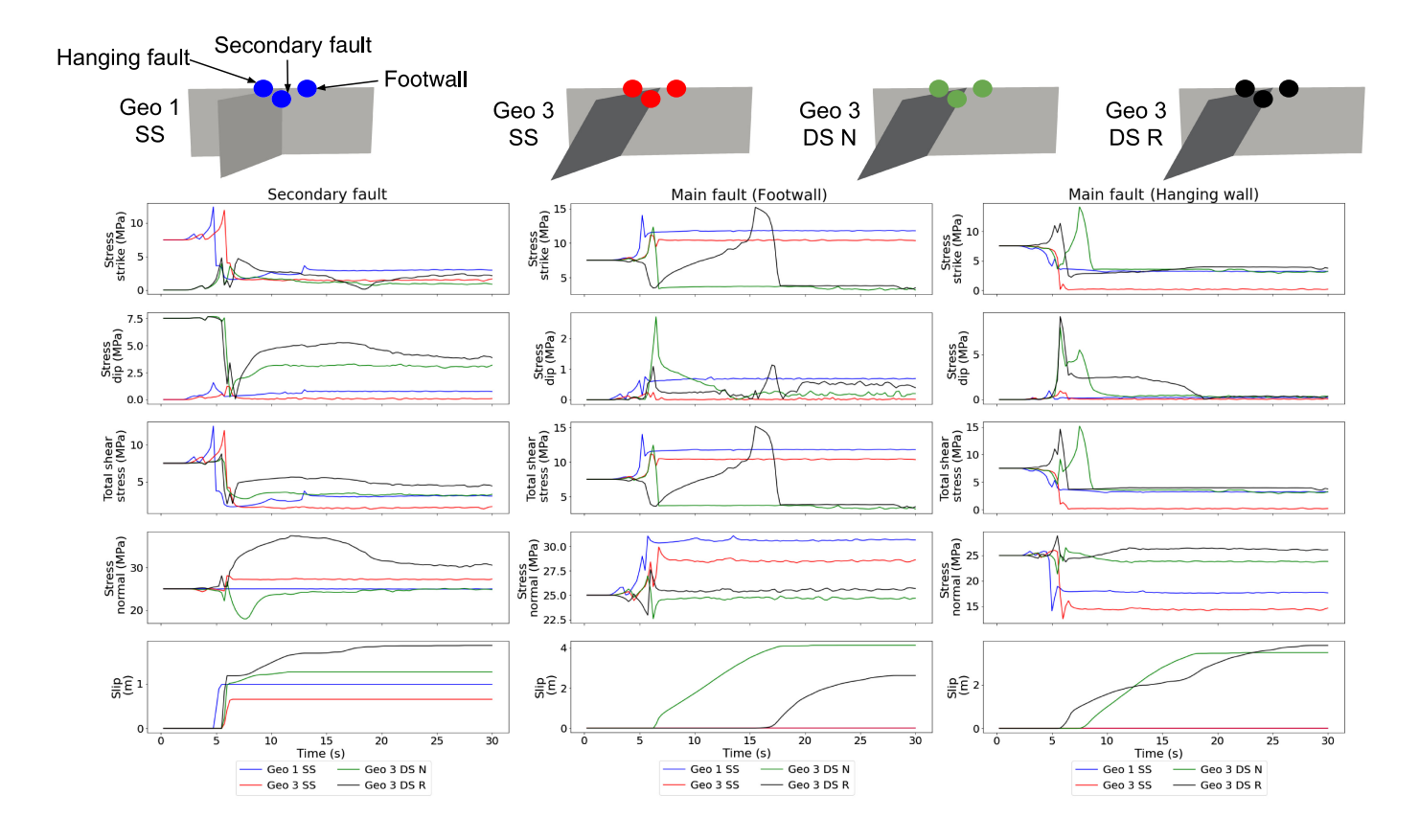
Impact of nucleation on a dipping secondary fault

In this study, we show that when rupture is nucleated on the secondary fault, even if the *S* value on the main fault is relatively high (greater than 2), the rupture is more likely to propagate through the branch intersection and onto the main fault when the secondary fault is shallowly dipping as opposed to

vertical or steeply dipping. This would suggest the stress state and rupture speed (low versus high S values) are not the only factors that can influence the rupture propagation. This would also imply that a dipping fault in interaction with the free surface can induce a stress effect on the fault system that can potentially facilitate the rupture to propagation across the junction similar to the on-fault stress perturbations observed when computing dynamic rupture simulation for a fault model with surface topography (Kyriakopoulos et al., 2021; Douilly, 2023). This stress effect on dip-slip faults was demonstrated in several stud-Oglesby et al. (1998, 2000) used rupture dynamics simulations to explore the dynamics of dipping faults. They found that the asymmetrical hanging-wall-footwall geometry of dipping faults causes free surface interactions which lead to normal stress changes and larger slip on the fault surface in comparison to vertical faults. This effect has later been well-documented in several studies (Duan and Oglesby, 2005; O'Connell et al., 2007; Ma and Beroza, 2008). More recently, Wu et al. (2023) used dynamic sim-

ulations to investigate the effects of burial depth on the proportionality constant *C*, which relates earthquake stress drop to slip magnitude (Kanamori and Anderson, 1975; Parsons *et al.*, 1988). They found that buried shallow-dipping thrust faults have a larger *C* value than thrust faults which rupture the free surface; indicating that for the same stress drop, a surface-rupturing thrust fault will have more slip than a buried thrust fault.

To isolate the effects of the dipping fault dynamics on the rupture along the branch system, we run additional scenarios on geometries 1 and 3 with a homogeneous stress condition instead of a regional stress field. For the following models, we assume a shear and normal stresses of 7.5 and 25 MPa, respectively, on all fault segments and we nucleate the rupture



on the secondary fault. Although we keep the magnitude of initial stresses fixed, we consider four different cases where we vary the rake angle of the shear stress only for the secondary fault while we keep the main fault the same with a pure along-strike shear stress. Figure 8 shows the results of the four cases with the fixed initial on-fault stresses: (1) geometry 13 with a strike-slip secondary fault, (2) geometry 3 with a strike-slip secondary fault, (3) geometry 3 with a normal secondary fault, and (4) geometry 3 with a reverse secondary fault. When we nucleate the rupture on the secondary fault, the rupture reaches the branch intersection for all four cases; however, it only propagates onto the main fault for cases 3 and 4. Although cases 1 and 2 have the same fault stress conditions and rupture did not propagate across both cases, case 2 experiences a reduction of normal stress on the main fault compared to case 1 (Figs. 8 and 9). Figure 9 shows the stress and slip evolutions for three points on the fault system near the branch intersection at 500 m depth: one point on the secondary fault, one point on the main fault to the footwall side of the secondary fault, and one point on the main fault to the hanging-wall side of the secondary fault. The stress perturbations observed in cases 2, 3, and 4 are analogous to the dynamic stress interactions with the free surface proposed by Oglesby et al. (1998) that cause an unclamping effect on the secondary fault which led to higher slip and more radiated energy. For case 3, the interaction between the free surface, the fault dip angle, and the normal motion on the fault induces a greater increase in slip on the secondary fault and a greater decrease in normal stress on the main fault that facilitates the rupture to jump across the branch system

Figure 9. Stress and slip evolution for three nodes near the branch intersection: one on the secondary fault, one on the main fault footwall side of the branch, and one on the main fault hanging wall side of the branch. For geometry 1 SS (purely left-lateral strike-slip) and geometry 3 SS (purely left-lateral strike-slip), the slip is constrained solely to the main fault (red and blue lines). For geometry 3 DS N (purely normal dip-slip), the main fault is brought to failure initially on the footwall side by a combination of a reduction in normal stress and an increase in shear stress in the dip direction (green lines). For geometry 3 DS R (purely reverse dip-slip), the main fault is initially brought to failure on the hanging-wall side by a large increase in shear stress in the dip direction (black line). The main fault only slips for cases with dip-slip motion on the secondary fault (Geo 3 DS N and Geo 3 DS R). The color version of this figure is available only in the electronic edition.

(Figs. 8 and 9). For case 4, the asymmetry between the hanging wall and footwall of the dipping fault causes rupture to initially propagate onto the hanging-wall side of the main fault. This behavior is consistent with results from previous studies on dip-slip faults (Oglesby et al., 1998, 2000), which highlight an increased particle motion of the hanging wall. This motion causes a significantly larger increase in shear stress in the dip direction for case 4 in comparison to the other cases, which causes the rupture in case 4 to initially propagate onto the hanging-wall side of the main fault (black line in Fig. 9 for the panel showing stress in the dip direction on the hanging-wall side).

Oglesby *et al.* (2000) and Wu *et al.* (2023) both argued that rupture on a buried dipping fault should lead to a decrease in slip and thus a decrease of the dynamic effects of the free surface on fault rupture as opposed to the surface-rupturing fault with the

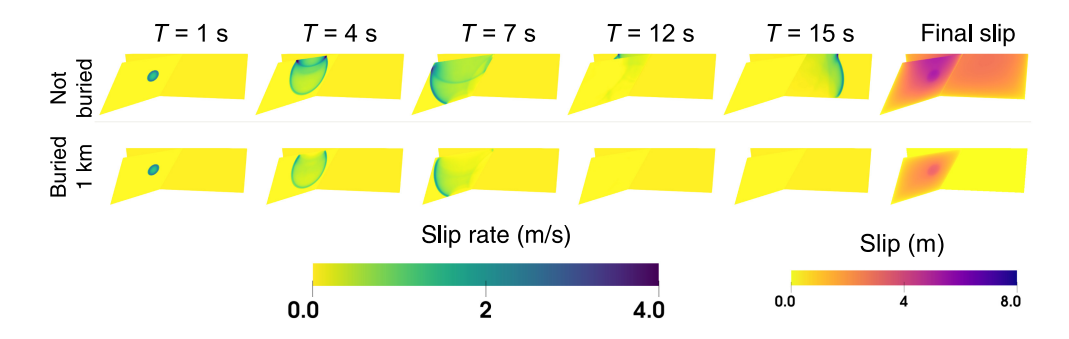


Figure 10. Snapshots of slip rate and final slip for two models of geometry 3 with a reverse secondary fault and left-lateral sense of slip on the main fault. In the top model (not buried), the rupture is allowed to reach the free surface and in the bottom model (buried 1 km), the fault system is buried 1 km beneath the free surface. The effects of the free surface can be seen at 4 s, with an increased slip rate in the top panel. Note that the rupture only propagates onto the main fault when it can rupture the free surface. The color version of this figure is available only in the electronic edition.

same dip angle and same stress drop. To test whether this decrease of the dynamic stress change could be enough to hinder throughgoing rupture, we then bury the secondary fault of geometry 3 to a depth of 1 km to prevent surface rupture (Fig. 9) and we assume the same stress conditions as in Figure 7. When we initiate the rupture on the secondary fault, as anticipated, the slip on the blind dipping fault is reduced compared to the non-buried case with the same stress conditions. This reduction in slip from the absence of the free surface rupturing effect leads to the rupture being fully constrained to the secondary fault segment (Fig. 10). Based on these results, we could argue that the free surface effect on dip-slip faults could potentially play a significant role as to why some earthquakes that nucleate on reverse secondary faults propagate onto adjacent strike-slip faults. A great example is the 2002 $M_{\rm w}$ 7.9 Denali earthquake which nucleated on the Susitna Glacier thrust fault and propagated onto the much longer right lateral Denali fault and later only continued on the Totschunda fault at the branch intersection (Eberhart-Phillips et al., 2003; Ratchkovski et al., 2004). Bhat et al. (2004) ran dynamic simulations across a branch fault system with a similar stressing angle as in that region. They argued that for a low branching angle and high stressing angle, a rupture initiated on the main fault will favor the extensional secondary and not the main fault regardless of the rupture speed. This explains why when the rupture reaches the branch intersection between the Denali fault and the Totschunda fault, the rupture continues to propagate only on the Taotschunda fault. However, this study did not explain why the rupture was able to jump from the Susitna Glacier thrust fault to the strike-slip Denali fault in the first place. During this event, there was a substantial surface rupture on the Susitna Glacier fault (Crone et al., 2004; Haeussler et al., 2004). The fault configuration of the Susitna Glacier thrust and the Denali fault is consistent with our geometry 3 for the high-stressing angle case. In that scenario, in addition to the fast rupture speed, the shallowly dipping secondary fault induces strong free surface effects that facilitate the rupture to jump

to the main fault consistently with the 2002 Denali rupture. This result agrees with the spontaneous dynamic models in Aagaard et al. (2004) that found that the orientation of the stress field and a shallow dipping angle of the Susitna Glacier thrust are necessary to replicate the throughgoing rupture to the Denali fault. This case study shows that our results have real hazard implications for future earthquake scenarios on the branch fault system. The free surface effect resulting from a dip-slip fault can have a signifi-

cant impact on the rupture path across the branch fault system, and we could even hypothesize that it would be more likely for a rupture to propagate from a secondary fault to the main fault if that secondary fault reaches the surface (not buried) and is shallowly dipping.

Sensitivity to other parameters

As mentioned earlier, other parameters may influence how rupture behaves at a branch intersection. In this section, we briefly discuss a few parameters and their relationship to this work.

Rupture speed. As stated in Kame et al. (2003) and Bhat et al. (2007), faster rupture speeds promote simultaneous throughgoing rupture on both the main and secondary faults. To investigate the effects of rupture speed in our models, we run additional models for geometries 2 and 3 where we vary the S value on the fault to change the rupture speed. For geometry 3 under the intermediate stressing angle ($\Psi = 40^{\circ}$), we increase the S value on the main fault from 0.39 (original value) to 0.85 by increasing the normal stress by 10%. When rupture is nucleated on the main fault, the higher S value reduces the rupture speed and results in the rupture only propagating on the main fault (Fig. 11). For geometry 2, we test two models where we increase the S value on the main fault to 0.85 by increasing the normal stress by 10% and one where we lower the S value to 0.22 by decreasing the normal stress by 5%. When we increase the S value to 0.85, the rupture speed decreases, and it does not propagate onto the secondary segment. For both S values of 0.39 and 0.22, the rupture triggers the secondary fault and quickly dies out (Fig. S1). However, the case with the lower S value of 0.22 develops more slip and has a faster rupture speed compared to the original one with the S value of 0.39. Finally, we run models for geometry 3 under the high stressing angle ($\Psi = 65^{\circ}$), where we increase the S value on the secondary fault from 0.32 (original value) to 1.35, 1.95, and 2.29 by increasing the normal stress by 50%, 70%, and 80%, respectively. Because we progressively

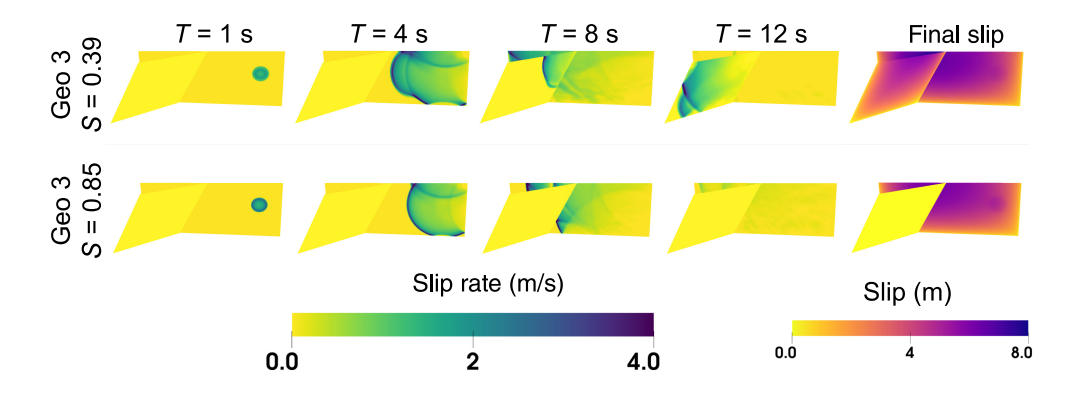


Figure 11. Snapshots of slip rate and final slip for geometry 3 for two different S values. Geo 3 with S=0.39 is the initial model run under the $\Psi=40^\circ$ stress orientation. Geo 3 with S=0.85 is also under the $\Psi=40^\circ$ stress orientation, but we increase the normal stress on the main by 10%. Geometry 3 with the higher S value, has a lower rupture speed when it reaches the branch intersection and does not propagate onto the S0 dipping secondary fault. The color version of this figure is available only in the electronic edition.

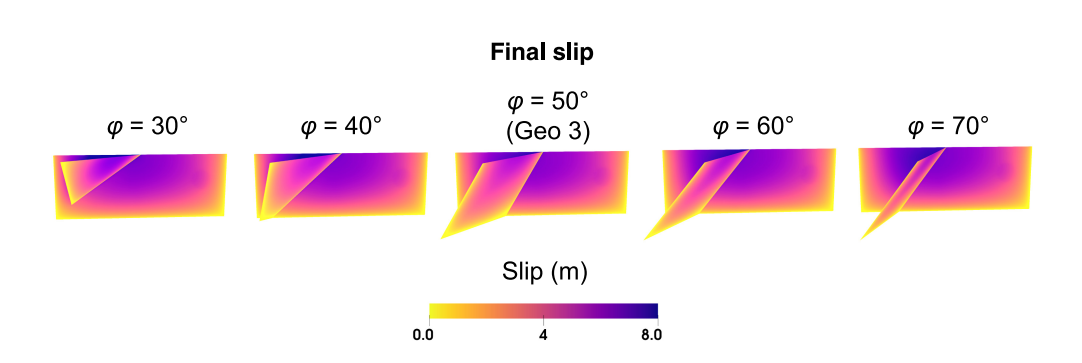


Figure 12. Final slip for geometries with different branch angles ranging from 30° to 70°. For each geometry the main fault is vertical, and the secondary fault is dipping at 55°. All models have the same initial on-fault stress conditions (equal to Table 3 row "geo 3" values). When rupture nucleates on the main fault, it propagates through the branch intersection on both the main and secondary fault. However, there are differences in slip magnitude, in particular, the narrowest branch angle of 30° causes the highest slip magnitude on the secondary fault. The color version of this figure is available only in the electronic edition.

increase the *S* values, the rupture speed decreases and less slip develops on the secondary fault until the rupture remains only on the secondary segment for the case with the *S* values of 2.29 (Fig. S2). We find that the argument of faster rupture speeds promoting throughgoing rupture and slower rupture speeds hindering it still holds for models with nonvertical dipping faults, independent of whether the rupture nucleates on the main or secondary fault.

Branching angle. We also run additional models with varying branch angles. In these models, the main fault is vertical and the secondary fault is dipping 55° toward the northwest, and we vary the intersection angle between the main and secondary fault from 30° to 70° by increments of 10°. For all these models, we assign on-fault stress conditions equal to the resolved stresses on geometry 3 for the intermediate stressing angle ($\Psi=40^\circ$). This ensures that the initial stress conditions are the same in all the

models and that any rupture differences are purely a result of the geometry of the branch angle. Final slip results for all five models indicate that under the prescribed initial conditions, the rupture propagates on both the main and secondary fault regardless of branch angle (Fig. 12). However, we do notice an interesting result in which the narrowest branch angle $(\varphi = 30^{\circ})$ yields the highest maximum slip amplitude on both the secondary fault and the east side of the main fault. This is likely due to a combination of factors. First, the main fault is strike-slip, whereas the secondary fault has a strong dip-slip component (see Table 3), this could minimize some of the stress shadowing effect. In addition, narrower branching angles can cause more dynamic stress interaction from wave propagation between the main and secondary fault (Aochi et al., 2000). Finally, the narrower angle between the faults leads to a smaller hanging-wall region which promote would increased motion due to the mass imbalance between the footwall and the hanging wall (Oglesby

et al., 2000; Ma and Beroza, 2008). We hypothesize that the interplay between these factors could lead to fundamental differences in expected rupture outcomes for narrow branching angles on vertical branch fault systems compared to dipping branch fault systems. Hopefully, future studies can shine a light on the interactions between fault branching angle, dynamic stressing from wave propagation, and hanging wall behavior for nonvertical branch fault systems.

Tensional versus compressional secondary fault. We also perform additional models for geometries 2 and 3 under the intermediate and high stressing angles, but with nucleation on the main fault west of the branch intersection to test the effects of tensional versus compressional secondary faults. For geometry 3 under the intermediate stressing angle ($\Psi=40^{\circ}$), when rupture nucleates on the main fault east of the branch intersection (nucleation 1), our results show that it ruptures

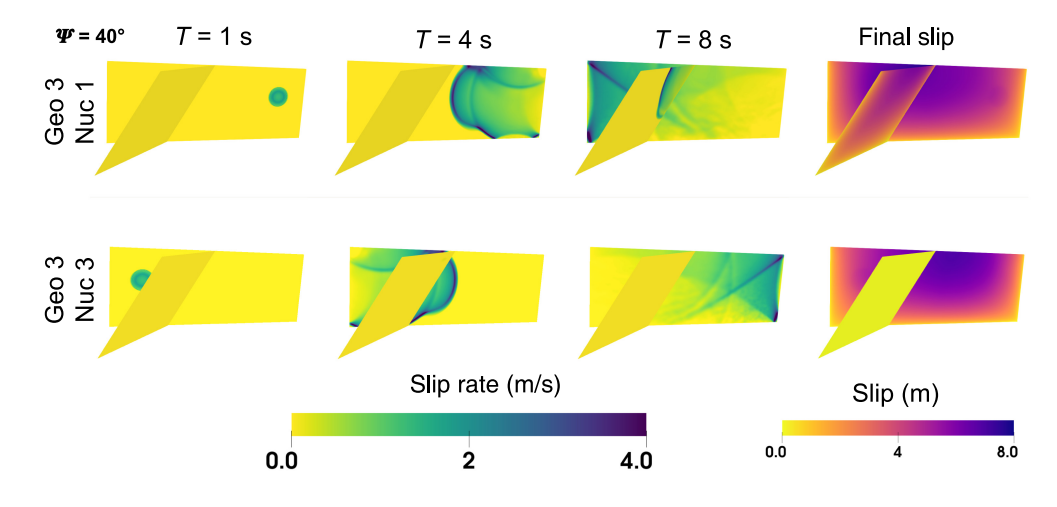


Figure 13. Snapshots of slip rate and final slip for geometry 3 with different nucleation locations under the $\Psi=40^\circ$ stressing angle (which yields a left-lateral sense of slip on the main fault). When the rupture nucleates in location Nuc 1 the rupture propagates onto the tensional secondary fault. However, when the rupture nucleates in location Nuc 3, the rupture remains solely on the main fault and does not rupture the compressional secondary fault. The color version of this figure is available only in the electronic edition.

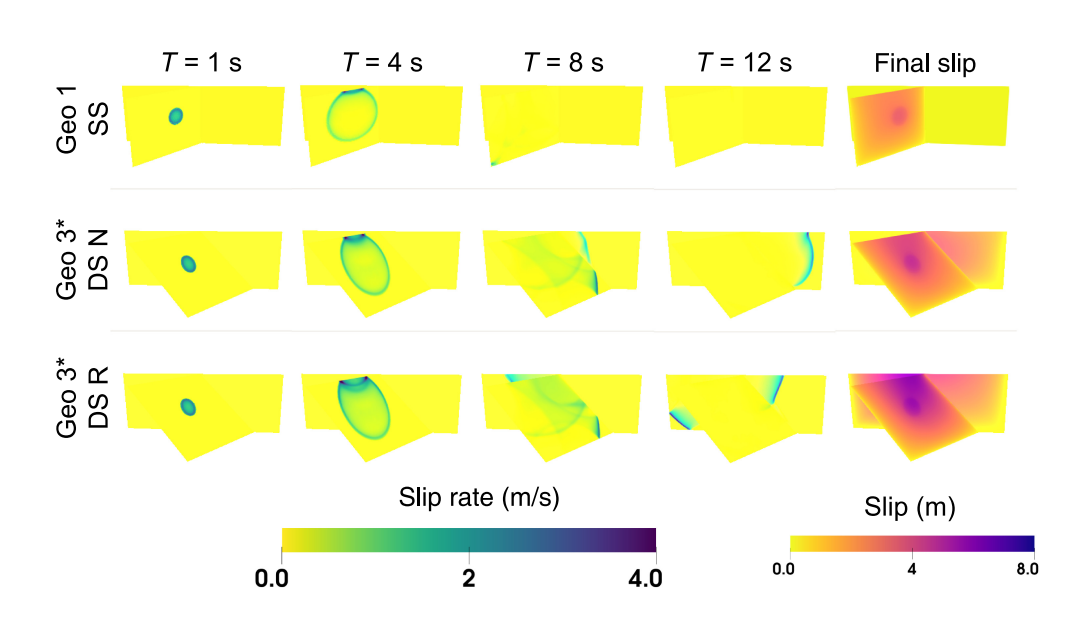


Figure 14. Snapshots showing slip rate and final slip for geometry 1 SS (purely left-lateral strike-slip), geometry 3*DS N (purely normal dip-slip), and geometry 3*DS R (purely reverse dip-slip) with 25 MPa normal stress and 7.5 MPa shear stress. For geometry 3*, the main fault is vertical and the secondary fault is dipping S55°E contrary to geometry 3, which has its secondary fault dipping N55°W. For geo 1, SS the rupture remains on the secondary fault. However, both dip-slip secondary faults promote throughgoing rupture onto the main fault. The color version of this figure is available only in the electronic edition.

the secondary segment; however when it nucleates on the west (nucleation 3), the rupture stays solely on the main fault (Fig. 13). Because the main fault is left lateral, nucleation east of the intersection (nucleation 1) leads to unclamping on the secondary fault, whereas nucleation on the west of the intersection (nucleation 3) leads to clamping on the secondary fault. We also observe similar behavior for geometries 2 and 3 under the high stress angle ($\Psi=65^{\circ}$). When rupture nucleates east of the

branch intersection, it ruptures the secondary tensional segment, but when it nucleates west of the intersection, it is constrained solely to the main fault (Figs. S3 and S4) and does not propagate to the compressional segment. Under both the intermediate and high stressing angles, the results are consistent with the vertical and 2D studies of Aochi et al. (2000) and Kame et al. (2003), that illustrating tensional branches are often favored over compressional branches even for nonvertical dipping faults.

direction. Earlier we Dip demonstrated that nucleation on dip-slip secondary faults promotes throughgoing rupture onto the main fault under uniform traction (Fig. 8). To test the sensitivity of our results to direction of the dip angle, we construct additional fault configurations, geometries 2* and 3*, which are equivalent to geometries 2 and 3, but with the secondary fault dipping toward the southeast instead of northwest. We consider the same uniform traction as in Figure 8 (shear stress magnitude of 7.5 MPa and normal stress of 25 MPa), and we nucleate the rupture on the 55° dipping secondary fault. We find that even if the secondary fault is dipping in the other direction, nucleation on a shallow dipping secondary fault still promotes throughgoing rupture onto the main fault compared to nuclea-

tion on a vertical strike-slip secondary fault (Fig. 14). Furthermore, we ran additional scenarios on geometries 2* and 3* for rupture nucleation on the secondary fault, using the same on-fault stress values from geometries 2 and 3 for the high stressing angle condition (Table 4, rows 2 and 3). Overall, we find that the final slip for the southeast dipping configurations is similar to the northwest configurations (Fig. S5). For geometry 2*, the rupture remains on the secondary fault just like we see for

geometry 2 in Figure 6, and for geometry 3*, the rupture propagates onto the main fault similarly to geometry 3. However, we do notice some small variations in rupture patterns among those geometries. As an example, although the rupture propagates the full extent of the main fault for both geometries 3 and 3*, it initially propagates along the main fault eastward for geometry 3 but westward for geometry 3* (see Fig. S5). This reversal of the delayed triggering pattern is directly linked to the change in dip direction from northwest to southeast and thus these results further emphasize the impact of fault dip angle and dip direction on rupture propagation across branch fault systems.

CONCLUSION

In this work, we present dynamic rupture model results illustrating the effects of dip angle on rupture along branch faults. We consider nine geometries, and we assume three distinct stressing angles ranging from low ($\Psi = 20^{\circ}$), intermediate ($\Psi = 40^{\circ}$), and high ($\Psi = 65^{\circ}$) inclination. For the low stressing angle, a rupture on the main fault is most likely to propagate across the branch intersection when the main fault is dipping and a rupture on the secondary fault will jump across for fast rupture speed (low S value) regardless of the dip angle of the main fault. For the intermediate stressing angle, a rupture on the main fault is most likely to propagate across the branch intersection when the secondary fault is dipping. For a high stressing angle, a rupture on the secondary fault is most likely to propagate to the main fault when the secondary fault is shallowly dipping. This is due to the fast rupture speed on the secondary fault and the induced stress effect that develops with the interaction of the free surface and a dipping fault. However, we also find that buried dipping secondary faults will reduce the free surface effect, which could hinder throughgoing rupture in comparison to surface rupturing faults. The results from this work can help understand the rupture behavior of several past earthquakes (i.e., the 2002 Denali earthquake, the 2010 and 2021 earthquakes in Haiti, and the 2023 Kahramanmaraş earthquake in Türkiye) that have occurred along branch fault systems with variable fault dip angle. Moreover, considering how stressing angle and fault dip angle have strong implications on throughgoing rupture across a branch fault system, future modeling studies should consider implementing accurate fault dip angles when assessing the likelihood of rupture propagation in complex fault systems.

DATA AND RESOURCES

This study is purely modeling and the authors did not make use of any observational data. However, select modeling outputs can be accessed at doi: 10.5281/zenodo.11390162. The Cubit meshing software can be purchased from https://coreform.com/. The finite-element code FaultMod (Barall, 2009) was used to compute the physics of the dynamic rupture process. The figures and videos were made using Paraview, which can be freely downloaded from https://www.paraview.org/. All websites were last accessed in January 2023. Videos of the slip evolution for the models can be found in the supplemental videos S1–S9.

DECLARATION OF COMPETING INTERESTS

The authors acknowledge that there are no conflicts of interest recorded.

ACKNOWLEDGMENTS

This research is supported by the Southern California Earthquake Center (SCEC) (Contribution Number 21084). SCEC is funded by National Science Foundation (NSF) Cooperative Agreement EAR-1600087 and U.S. Geological Survey (USGS) Cooperative Agreement G17AC000047. Figures were generated using Paraview (http://www.paraview.org/, last accessed September 2022). The authors are grateful to Julian Lozos and an anonymous reviewer for their thoughtful and constructive feedback which improved the article and figures. The authors thank David Oglesby and Baoning Wu for their fruitful discussions that helped advance this study. Computations were performed using the computer clusters and data storage resources of the High Performance Computing Cluster (HPCC) at UC Riverside, which were funded by grants from NSF (MRI-2215705, MRI-1429826) and National Health Institute (NIH) (1S10OD016290-01A1).

REFERENCES

- Aagaard, B. T., G. Anderson, and K. W. Hudnut (2004). Dynamic rupture modeling of the transition from thrust to strike-slip motion in the 2002 Denali Fault Earthquake, Alaska, *Bull. Seismol. Soc. Am.* **94,** no. 6B, S190–S201, doi: 10.1785/0120040614.
- Aki, K. (1967). Scaling law of seismic spectrum, J. Geophys. Res. 72, no. 4, 1217–1231.
- Andrews, D. (1976). Rupture velocity of plane strain shear cracks, *J. Geophys. Res.* **81**, no. 32, 5679–5687.
- Aochi, H., E. Fukuyama, and M. Matsu'ura (2000). Selectivity of spontaneous rupture propagation on a branched fault, *Geophys. Res. Lett.* **27**, no. 22, 3635–3638.
- Aochi, H., R. Madariaga, and E. Fukuyama (2002). Effect of normal stress during rupture propagation along nonplanar faults, *J. Geophys. Res.* **107**, no. B2, doi: 10.1029/2001JB000500.
- Archuleta, R. J. (1982). Hypocenter for the 1979 Imperial Valley earthquake, *Geophys. Res. Lett.* **9**, no. 6, 625–628.
- Archuleta, R. J. (1984). A faulting model for the 1979 Imperial Valley earthquake, *J. Geophys. Res.* **89**, no. B6, 4559–4585.
- Bai, K., and J.-P. Ampuero (2017). Effect of seismogenic depth and background stress on physical limits of earthquake rupture across fault step overs, *J. Geophys. Res.* **122**, no. 12, 10,280–10,298.
- Barall, M. (2009). A grid-doubling finite-element technique for calculating dynamic three-dimensional spontaneous rupture on an earthquake fault, *Geophys. J. Int.* **178**, no. 2, 845–859.
- Barbot, S., H. Luo, T. Wang, Y. Hamiel, O. Piatibratova, M. T. Javed, C. Braitenberg, and G. Gurbuz (2023). Slip distribution of the February 6, 2023 $M_{\rm w}$ 7.8 and $M_{\rm w}$ 7.6, Kahramanmaraş, Turkey earthquake sequence in the east Anatolian fault zone, *Seismica* 2, no. 3, doi: 10.26443/seismica.v2i3.502.
- Bhat, H. S., R. Dmowska, J. R. Rice, and N. Kame (2004). Dynamic slip transfer from the Denali to Totschunda faults, Alaska: Testing theory for fault branching, *Bull. Seismol. Soc. Am.* **94**, no. 6B, S202–S213.
- Bhat, H. S., M. Olives, R. Dmowska, and J. R. Rice (2007). Role of fault branches in earthquake rupture dynamics, *J. Geophys. Res.* **112**, no. B11, doi: 10.1029/2007JB005027.

- Calais, E., A. Freed, G. Mattioli, F. Amelung, S. Jónsson, P. Jansma, S.-H. Hong, T. Dixon, C. Prépetit, and R. Momplaisir (2010).
 Transpressional rupture of an unmapped fault during the 2010 Haiti earthquake, *Nature Geosci.* 3, no. 11, 794–799.
- Crone, A. J., S. F. Personius, P. A. Craw, P. J. Haeussler, and L. A. Staft (2004). The Susitna Glacier thrust fault: Characteristics of surface ruptures on the fault that initiated the 2002 Denali fault earthquake, *Bull. Seismol. Soc. Am.* 94, no. 6B, S5–S22.
- Das, S., and K. Aki (1977). A numerical study of two-dimensional spontaneous rupture propagation, *Geophys. J. Int.* **50**, no. 3, 643–668.
- Day, S. M. (1982). Three-dimensional simulation of spontaneous rupture: The effect of nonuniform prestress, *Bull. Seismol. Soc. Am.* 72, no. 6A, 1881–1902.
- Douilly, R. (2023). Effect of asymmetric topography on rupture propagation along fault stepovers, *J. Geophys. Res.* **128**, no. 7, e2023JB026484, doi: 10.1029/2023JB026484.
- Douilly, R., J. S. Haase, W. L. Ellsworth, M.-P. Bouin, E. Calais, S. J. Symithe, J. G. Armbruster, B. M. de Lépinay, A. Deschamps, and S.-L. Mildor (2013). Crustal structure and fault geometry of the 2010 Haiti earthquake from temporary seismometer deployments crustal structure and fault geometry of the 2010 Haiti earthquake from temporary seismometer deployments, *Bull. Seismol. Soc. Am.* 103, no. 4, 2305–2325.
- Douilly, R., D. D. Oglesby, M. L. Cooke, and J. L. Hatch (2020). Dynamic models of earthquake rupture along branch faults of the eastern San Gorgonio Pass region in California using complex fault structure, *Geosphere* **16**, no. 2, 474–489.
- Duan, B., and D. D. Oglesby (2005). The dynamics of thrust and normal faults over multiple earthquake cycles: Effects of dipping fault geometry, *Bull. Seismol. Soc. Am.* **95**, no. 5, 1623–1636.
- Duan, B., and D. D. Oglesby (2007). Nonuniform prestress from prior earthquakes and the effect on dynamics of branched fault systems, *J. Geophys. Res.* **112**, no. B5, doi: 10.1029/2006JB004443.
- Eberhart-Phillips, D., P. J. Haeussler, J. T. Freymueller, A. D. Frankel, C. M. Rubin, P. Craw, N. A. Ratchkovski, G. Anderson, G. A. Carver, and A. J. Crone (2003). The 2002 Denali fault earthquake, Alaska: A large magnitude, slip-partitioned event, *Science* 300, no. 5622, 1113–1118.
- Freitag, L. A., and P. M. Knupp (2002). Tetrahedral mesh improvement via optimization of the element condition number, *Int. J. Numer. Methods Eng.* **53**, no. 6, 1377–1391.
- Fuis, G. S., D. S. Scheirer, V. E. Langenheim, and M. D. Kohler (2012).
 A new perspective on the geometry of the San Andreas fault in southern California and its relationship to lithospheric structure,
 Bull. Seismol. Soc. Am. 102, no. 1, 236–251.
- Haeussler, P. J., D. P. Schwartz, T. E. Dawson, H. D. Stenner, J. J. Lienkaemper, B. Sherrod, F. R. Cinti, P. Montone, P. A. Craw, and A. J. Crone (2004). Surface rupture and slip distribution of the Denali and Totschunda faults in the 3 November 2002 M 7.9 earthquake, Alaska, *Bull. Seismol. Soc. Am.* 94, no. 6B, S23–S52.
- Harris, R. A., and S. M. Day (1999). Dynamic 3D simulations of earth-quakes on en echelon faults, *Geophys. Res. Lett.* **26**, no. 14, 2089–2092.
- Harris, R. A., R. J. Archuleta, and S. M. Day (1991). Fault steps and the dynamic rupture process: 2D numerical simulations of a spontaneously propagating shear fracture, *Geophys. Res. Lett.* **18**, no. 5, 893–896.

- Harris, R. A., M. Barall, B. Aagaard, S. Ma, D. Roten, K. Olsen, B. Duan, D. Liu, B. Luo, and K. Bai (2018). A suite of exercises for verifying dynamic earthquake rupture codes, *Seismol. Res. Lett.* 89, no. 3, 1146–1162.
- Harris, R. A., M. Barall, R. Archuleta, E. Dunham, B. Aagaard, J. P. Ampuero, H. Bhat, V. Cruz-Atienza, L. Dalguer, P. Dawson, et al. (2009). The SCEC/USGS dynamic earthquake rupture code verification exercise, Seismol. Res. Lett. 80, no. 1, 119–126.
- Ida, Y. (1972). Cohesive force across the tip of a longitudinal-shear crack and Griffith's specific surface energy, *J. Geophys. Res.* 77, no. 20, 3796–3805.
- Kadinsky-Cade, K., and A. A. Barka (1989). Effects of restraining bends on the rupture of strike-slip earthquakes. Fault segmentation and controls of rupture initiation and termination, U.S. Geol. Surv. Open-File Rept. 89-315, 181–192.
- Kame, N., J. R. Rice, and R. Dmowska (2003). Effects of prestress state and rupture velocity on dynamic fault branching, *J. Geophys. Res.* **108**, no. B5, doi: 10.1029/2002JB002189.
- Kanamori, H. (1978). Quantification of earthquakes, *Nature* 271, no. 5644, 411–414.
- Kanamori, H., and D. L. Anderson (1975). Theoretical basis of some empirical relations in seismology, *Bull. Seismol. Soc. Am.* 65, no. 5, 1073–1095.
- Kleffmann, S., F. Davey, A. Melhuish, D. Okaya, T. Stern, and S. Team (1998). Crustal structure in the central South Island, New Zealand, from the Lake Pukaki seismic experiment, *New Zeal. J. Geol. Geophys.* **41,** no. 1, 39–49.
- Knupp, P. M. (2000). Achieving finite element mesh quality via optimization of the Jacobian matrix norm and associated quantities. Part II—A framework for volume mesh optimization and the condition number of the Jacobian matrix, *Int. J. Numer. Meth. Eng.* 48, no. 8, 1165–1185.
- Kyriakopoulos, C., B. Wu, and D. D. Oglesby (2021). Asymmetric topography causes normal stress perturbations at the rupture front: The case of the Cajon pass, *Geophys. Res. Lett.* **48**, no. 20, e2021GL095397, doi: 10.1029/2021GL095397.
- Lozos, J. C., D. D. Oglesby, B. Duan, and S. G. Wesnousky (2011). The effects of double fault bends on rupture propagation: A geometrical parameter study, *Bull. Seismol. Soc. Am.* 101, no. 1, 385–398.
- Ma, S., and G. C. Beroza (2008). Rupture dynamics on a bimaterial interface for dipping faults, *Bull. Seismol. Soc. Am.* **98**, no. 4, 1642–1658.
- Ma, X., and A. Elbanna (2019). Dynamic rupture propagation on fault planes with explicit representation of short branches, *Earth Planet. Sci. Lett.* **523**, 115702, doi: 10.1016/j.epsl.2019.07.005.
- Melgar, D., T. Taymaz, A. Ganas, B. W. Crowell, T. Öcalan, M. Kahraman, V. Tsironi, S. Yolsal-Çevikbil, S. Valkaniotis, and T. S. Irmak (2023). Sub-and super-shear ruptures during the 2023 $M_{\rm w}$ 7.8 and $M_{\rm w}$ 7.6 earthquake doublet in SE Türkiye, doi: 10.31223/X52W9D.
- O'Connell, D. R., S. Ma, and R. J. Archuleta (2007). Influence of dip and velocity heterogeneity on reverse-and normal-faulting rupture dynamics and near-fault ground motions, *Bull. Seismol. Soc. Am.* **97**, no. 6, 1970–1989.
- Oglesby, D. D. (2005). The dynamics of strike-slip step-overs with linking dip-slip faults, *Bull. Seismol. Soc. Am.* **95**, no. 5, 1604–1622.

- Oglesby, D. D., R. J. Archuleta, and S. B. Nielsen (1998). Earthquakes on dipping faults: The effects of broken symmetry, *Science* **280**, no. 5366, 1055–1059.
- Oglesby, D. D., R. J. Archuleta, and S. B. Nielsen (2000). The three-dimensional dynamics of dipping faults, *Bull. Seismol. Soc. Am.* **90**, no. 3, 616–628.
- Parsons, I. D., J. F. Hall, and G. A. Lyzenga (1988). Relationships between the average offset and the stress drop for two-and threedimensional faults, *Bull. Seismol. Soc. Am.* 78, no. 2, 931–945.
- Poliakov, A. N., R. Dmowska, and J. R. Rice (2002). Dynamic shear rupture interactions with fault bends and off-axis secondary faulting, *J. Geophys. Res.* **107**, no. B11, ESE 6-1-ESE 6-18.
- Pousse-Beltran, L., E. Nissen, E. A. Bergman, M. D. Cambaz, É. Gaudreau, E. Karasözen, and F. Tan (2020). The 2020 $M_{\rm w}$ 6.8 Elazığ (Turkey) earthquake reveals rupture behavior of the east Anatolian fault, *Geophys. Res. Lett.* 47, no. 13, e2020GL088136, doi: 10.1029/2002JB002189.
- Ratchkovski, N. A., S. Wiemer, and R. A. Hansen (2004). Seismotectonics of the central Denali fault, Alaska, and the 2002 Denali fault earthquake sequence, *Bull. Seismol. Soc. Am.* **94**, no. 6B, S156–S174.
- Romanet, P., D. S. Sato, and R. Ando (2020). Curvature, a mechanical link between the geometrical complexities of a fault:

- Application to bends, kinks and rough faults, *Geophys. J. Int.* **223**, no. 1, 211-232.
- Sibson, R. H., S. Das, J. Boatwright, and C. H. Scholz (1986). Rupture interaction with fault jogs, *Earthq. Source Mech.* 37, 157–167.
- Sibson, R. H., S. H. White, and B. K. Atkinson (1981). Structure and Distribution of Fault Rocks in the Alpine Fault Zone, New Zealand,
- Vol. 9, Geological Society, London, Special Publications, 197–210.
 Stern, T., D. Okaya, S. Kleffmann, M. Scherwath, S. Henrys, and F. Davey (2007). Geophysical exploration and dynamics of the Alpine fault zone, AGU (American Geophysical Union), San Francisco, California, 10–14 December 2007.
- Woodcock, N. H., and M. Fischer (1986). Strike-slip duplexes, J. Struct. Geol. 8, no. 7, 725–735.
- Wu, B., C. Kyriakopoulos, D. D. Oglesby, and K. J. Ryan (2023). Variation of proportionality between stress drop and slip, with implications for megathrust earthquakes, *Geophys. Res. Lett.* 50, no. 4, e2022GL100568, doi: 10.1029/2022GL100568.

Manuscript received 15 February 2024
Published online 16 October 2024